Production and characterization of nanostructured materials for optical applications at Rovira i Virgili University

Joan J. Carvajal, Magdalena Aguiló, Francesc Díaz*

Física i Cristal·lografia de Materials (FiCMA), Universitat Rovira i Virgili (URV),Tarragona

Resum

Quan la mida de materials òptics ben coneguts es redueix al rang dels nanómetres, apareixen noves propietats físiques. Això ha motivat l'aparició d'un gran interès per la síntesi i la caracterització d'aquests nanocristalls, cobrint tots els vessants, des dels materials amb aplicacions làser fins als materials per fenòmens de conversió de freqüència. En aquesta publicació, presentem tres noves estratègies en l'estudi d'aquests materials desenvolupades els últims anys als laboratoris del nostre grup de recerca. Les noves característiques espectroscòpiques dels nanocristalls han impulsat al nostre grup a l'estudi de nous procediments de síntesi de tungstats dobles i també de sesquiòxids, ambdós contenint ions lantànids, a partir de tècniques de sol-gel. Els nanocristalls obtinguts han estat caracteritzats estructuralment, morfològicament, fonónicament i espectroscòpica amb la intenció de fabricar nous materials ceràmics amb òptimes prestacions làser.

L'explotació de les oportunitats tecnològiques que ofereixen les propietats de les estructures uni-dimensionals de semiconductors de *gap* ample també estan sent objecte d'estudi en el nostre grup de recerca. En aquest context, s'han sintetitzat *rods* de mides sub-micromètriques de GaN dopats amb Er, crescuts sobre substrats de silici (001) mitjançant la reacció directa entre el gali i l'amoníac en un sistema de deposició química en fase vapor. Les propietats espectroscòpiques d'aquests *rods* de mides sub-micromètriques s'han estudiat per entendre els mecanismes d'excitació dels ions lantànids en aquestes estructures de semiconductors, que podrien proporcionar emissions òptiques tecnològicament molt demandades. En aquests *rods* de mides sub-micromètriques s'han observat emissions en el verd i en el vermell a temperatura ambient mitjançant excitació per sota de l'energia del *gap* del semiconductor. Finalment, la formació de conjunts ordenats d'aquestes estructures uni-dimensional es especialment interessant degut a les noves pro-

* Author for correspondence: F. Díaz. Física i Cristal·lografia de Materials (FiCMA), Departament de Química Física i Inorgànica, Facultat de Química, Universitat Rovira i Virgili (URV). Campus Sescelades, c/ Marcel·lí Domingo, s/n. 43007 Tarragona, Catalonia, EU.
Tel. +34 977559517. Fax +34 977559563. E-mail: f.diaz@urv.cat

Abstract

Novel physical properties arise when the size of well-established optical materials is decreased to the nanometer range. This has generated great interest in all aspects of the synthesis and characterization of such nanocrystals, from materials for laser applications to materials for frequency conversion phenomena. In this paper we present three new approaches for studying these materials. Nanocrystals of laser materials are expected to show new spectroscopic features compared to their bulk counterparts. This has led to advances in the procedures for the synthesis of nanocrystals of double potassium tungstates and lutetium sesquioxides, both containing lanthanide ions, using a sol-gel approach: the Pechini method. We extensively characterize the structure and spectra of these new nanocrystals with the aim of facilitating the production of new ceramic materials with laser applications. We also analyze the morphology and vibrational structures of the nanoparticles produced. We synthesized also Er-doped GaN sub-micron-sized rods on silicon (001) through the direct reaction of gallium and ammonia in a simple chemical vapor deposition system. This allowed us to study the unique properties that natural electron confinement leads to in such wide-bandgap semiconductors. We studied their spectroscopic properties in depth to understand the excitation mechanisms of lanthanide ions in such semiconductor structures, which can lead to nearly ideal optical emissions. We recorded green and red emissions at room temperature coming from sub-micron-sized rods with excitation below the energy of the bandgap. Finally, the formation of ordered arrays of these one-dimensional structures is of special interest due to the new properties that may arise when compared to individual one-dimensional structures. At the *Física i Cristal·lografia de Materials* laboratory at *Universitat Rovira i Virgili (URV)* we produced two-dimensional photonic crystals of $KTiOPO_4$, a non-linear optical material, using an entirely new procedure that combines bottom-up and top-down approaches. We produced an ordered array of $KTiOPO_4$ one-dimensional structures using a silicon macroporous template and a $KTiOPO_4$ substrate to control their orientation. We demonstrated the physical properties of these photonic crystals: we meas-

pietats que poden aparèixer quan es comparen a les propietats que presenten els components d'aquests conjunts de forma independent. Als nostres laboratoris de Física i Cristal·lografia de Materials (FiCMA) de la Universitat Rovira i Virgili (URV) s'estan fabricant actualment cristalls fotònics bidimensionals de materials d'òptica no-lineal, com el $KTiOPO_4$, mitjançant nous procediments que combinen metodologies d'enfocament de baix a dalt i d'enfocament de dalt a baix. El conjunt ordenat d'estructures uni-dimensionals de $KTiOPO_4$ és fabriquen mitjançant l'utilització d'un patró de silici macroporós i un substrat de $KTiOPO_4$ que controla l'orientació de creixement de les estructures uni-dimensionals. Les propietats físiques d'aquest cristall fotònic han estat mesurades, la seva banda prohibida de tercer ordre determinada i també avaluades les seves propietats de difracció amb llum visible i IR.

ured their third-order forbidden band, and explored their near-IR and visible light diffraction properties.

1. Introduction

In the field of optical materials, new perspectives related to nanoscience and nanotechnology are derived from the novel properties of some well-known optical materials when they are synthesized on the nanometer scale. Certain physical properties, such as those related to spectroscopic or non-linear optical parameters, are affected by the size of the sample [1]. This has generated great interest in the synthesis and characterization of nanocrystals of a wide range of well-known optical materials, from laser materials to non-linear optical materials.

In laser materials, interest in nanocrystals centers on the spectroscopic features that are new compared to those of their bulk counterparts. Spectroscopic properties are different at such a small scale partly due to the high surface-volume ratio [2,3]. Currently, ceramics produced by sintering nanocrystals are being extensively researched, with the idea of using them in the field of opto-electronics and modern quantum electronics as interesting and novel lasing materials. As reported in the literature [4], larger samples of laser ceramics can be obtained more economically than conventional single crystalline materials. The sintering temperatures used for the production of such ceramics are usually lower than the melting or crystal growth temperatures required for producing single crystalline materials. Thus, theoretically, ceramics are easier to produce than good single crystals. The main challenge for the production of these new laser materials lies in the preparation of optically transparent ceramics, which is related to the sintering process. The activation of such sintering processes is enhanced when the grains that will form the ceramic have dimensions in the nano range. It is therefore highly desirable to understand accurately the synthesis processes leading to high-quality nanocrystals or nanopowders, from which new laser ceramics will be produced. A common technology for producing such nanocrystals or nanopowders of inorganic materials is based on the sol-gel method.

Sol-gel technology, by which composite organic-inorganic materials are made at relatively low temperatures, involves the hydrolysis of the constituent molecular precursors and subsequent polycondensation in a glass-like form [5]. Sol-gel methods allow homogenous samples to be obtained at low temperatures, and the starting cationic composition to be controlled using metal salts mixed in a liquid solution as initial reagents.

Recently, much effort has been directed towards the synthesis of one-dimensional nanostructures. They constitute ideal systems for confining electrons, and by controlling their diameter the effect on their fundamental physical properties can be studied. This is as true of optical materials as of any other type Several studies of one-dimensional semiconductor nanostructures have examined how they function in different devices such as, LEDs, diode lasers, and FETs [6]. The synthesis of one-dimensional semiconductor structures doped with optically active ions—such as lanthanide (Ln) ions—is of special interest for the production of new phosphors, and also for studying the excitation mechanisms of lanthanide ions in such structures. The photoemission generated by Ln ions when introduced into semiconductors has been limited due to both the low solubility of Ln in semiconductors, and severe temperature quenching at room temperature [7]. However, this thermal quenching has been reported to decrease as the bandgap of the semiconductor increases [8]. So, wide-bandgap semiconductors have become more attractive hosts for Ln ions. Additionally, when such semiconductors possess a direct bandgap, it is possible to electrically excite the Ln ions with hot carriers through impact excitation, or as a result of nearby electron-hole recombination. These mechanisms can generate near-ideal optical emissions, which can be properly amplified [9].

The formation of arrays of such one-dimensional structures is of particular interest. Controlling the position of these nanowires and nanorods during synthesis, and studying the new properties of an array compared to those of individual one-di-

mensional structures are two current goals of research. In particular, a photonic crystal (PC; an ordered structure whose refractive index varies periodically throughout the structure) is ideal for controlling non-linear optical interactions. These crystals may enhance [10] [11] [12], phase match [13] [14], or cause a non-vanishing second-order interaction with an incident beam of light even if the material is centrosymmetric [15]. For instance, the structure of the dielectric material together with the modulation of the second-order non-linear susceptibility may lead to a backward parametric oscillation [16]. This is a non-linear effect that was predicted many years ago but has yet to be demonstrated experimentally. Among all the possible PC structures, 2D PCs are, perhaps, the most interesting. They can easily be integrated into optoelectronic devices designed to amplify light, generate light at changed frequencies, process optical data, or act as sensors [17] [18] [19] [20].

In recent years, our research group at the *Física i Cristal·lografia de Materials* Laboratory of *Universitat Rovira i Virgili* (FiCMA) has developed techniques and procedures for producing and characterizing oxide nanocrystals which can be used in laser applications, wide-bandgap semiconductor nanostructures doped with lanthanide ions, and both microwire and nanowire non-linear optical arrays (PCs). In the present paper we describe our most important results in these areas.

2. Synthesis of oxide nanocrystals for laser applications

For more than ten years we have studied the monoclini $KRE(WO_4)_2$ family of laser materials. Production of bulk single crystals by the high-temperature solution growth method has been optimized at the FiCMA [21] [22] [23] [24]. The physical properties of KREW materials are governed by their huge degree of anisotropy. Optically, monoclinic KREW are biaxial crystals. Their thermal conductivity and linear thermal expansion are anisotropic, and also depend on the RE^{3+} cation [25]. Their anisotropy gives rise to large absorption and emission cross sections of the active ions.

The rare earth sesquioxides, RE_2O_3, are excellent laser hosts [26,27]. Sesquioxides such as Sc_2O_3, Y_2O_3 and Lu_2O_3 exhibit very high thermal conductivity [28] and can be heavily doped with lanthanide ions. Lu_2O_3 belongs to the cubic system; space group *Ia3* and unit cell parameter a = 1.039 nm with Z = 16 [29]. Its high melting point (around 3213 K) makes it difficult to grow Lu_2O_3 crystals from molten solutions [25]. It is an excellent host for ytterbium ions because of the similar ionic radii and masses of Yb^{3+} and Lu^{3+}. Its isotropic optical properties potentially make it a highly suitable compound for obtaining extremely transparent laser ceramics.

The modified Pechini method developed as a sol-gel technique consists of initially preparing a precursor polymer resin in which the metals are complexed, and then calcining this precursor resin to obtain the desired nanocrystals. Figure 1 shows the main steps in this procedure. First, a mixture of cations is formed in citric acid, as an organic complexing agent (CA) and ethylene glycol (EG) solution. Second, the cations form a chelant. Third, the polymeric resin is formed; and finally it decomposes when heated. More detailed explanations can be found in [30].

Powders of precursor oxides for each compound—K_2CO_3 (Fluka, 99.0%), RE_2O_3 (Aldrich, 99.9%) and ammonium (para) tungstate $(NH_4)_{10}W_{12}O_{41} \cdot 7H_2O$ (Riedel-de Häen, 99%) for KREW nanocrystals; and Lu_2O_3 (Aldrich, 99.9%) for Lu_2O_3 nanocrystals—were used as starting materials. These precursor oxides were dissolved in concentrated HNO_3 to obtain a nitrate solution. The solid residue was then obtained by complete evaporation at 373 K.

From three molar quantities of metal cations [Metal] together with [CA] and [EG], two molar ratios can be defined: CM = [CA]/[Metal] and CE = [CA]/[EG]. The microstructure of the solid residue is related with these two ratios. CM describes the degree of chelation of the metal in the organic product. CE describes the degree of esterification between the chelating agent and EG. Two organic compounds can be used as chelating agents: concentrated citric acid solution, and EDTA. EDTA has a stronger chelate effect than citric acid and is more commonly used.

The solid residue is then dissolved in concentrated EDTA solution (99.9%), as described by CM. To produce esterification (as described by CE) we then added EG. Resin is formed at 363 K. During this reaction resin gels form which are then dried to yield the precursor polymeric resin.

The last step of the process is the calcination of the dried polymeric resin at high temperatures in air for several hours. This calcination step has been optimized (in terms of temperature and time) for each compound, to obtain equally-sized nanocrystals. The lower the temperature, the smaller the crystallite sizes: at higher temperatures the rates of crystal growth and molecular diffusion are enhanced, which fuses the small crystallites and leads to the formation of well-defined larger crystals.
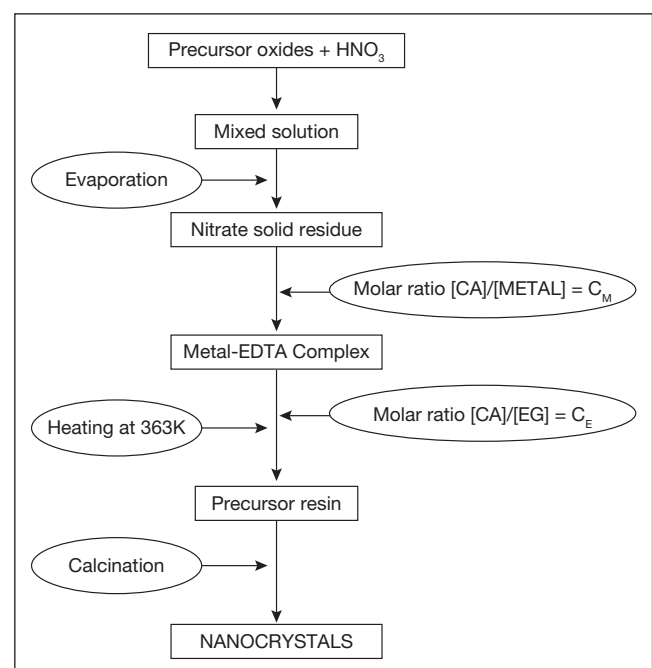

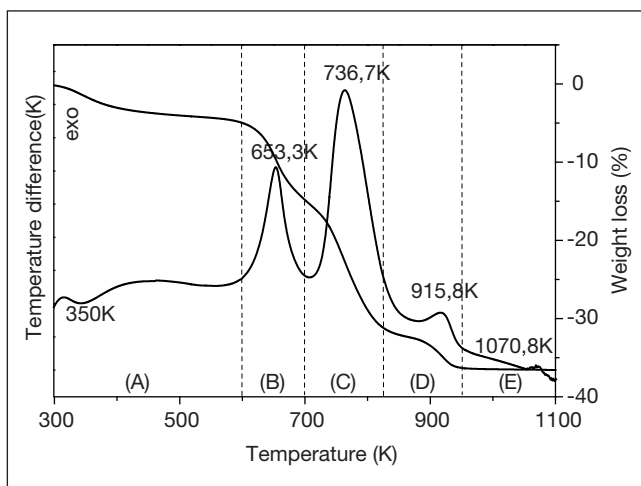Figure 1. Flow diagram of the Pechini method

Figure 2. DTA-TG analysis of precursor resin for obtaining Yb:Lu₂O₃ nanocrystals by the modified Pechini method

The thermal decomposition of the precursor polymeric resin during calcination was characterized by thermal analysis and X-ray powder diffraction. Thermal analysis was conducted using a DTA-TG instrument (TA Instruments, SDT 2960: simultaneous differential techniques instrument) in an air flow at a heating rate of 10 K/min. Al_2O_3 powder was used as the reference material. X-ray powder diffraction was performed on the powder obtained by different calcination temperatures using a Siemens D-5000 diffractometer with a θ-θ configuration.

To interpret the results, it is necessary to know the behavior of the initial organic reagents. EDTA decomposes endothermically between 500 and 550 K in one step, and its derivatives ignite at around 780 K. Pure EG would present a strong endothermic peak at the beginning of the boiling process: around 471 K [31]. As an example, Figure 2 shows the DTA curves for the $Yb:Lu_2O_3$ precursor polymeric resin. Five steps associated with weight losses can be observed in the DTA/TG curve. In the first, A, the temperature interval and weight loss were 300-600 K and 5%. This weight loss is due to the evaporation of water produced in the esterification reaction between the EDTA and EG. It shows a weak endothermic peak at around 350 K in the DTA thermogram. In the second stage, B, from 600 to 700 K, the weight loss is around 10%. The DTA curve shows one exothermic peak at 653 K, which corresponds to the evaporation of the organic solvent, EG. In stage C (700-825 K, weight loss = 16%) the exothermic peak at 736.7 K results from the oxidation of the residual organic compounds. The next exothermic peak is at 915.8 K (in stage D: 825-950 K) and corresponds to crystallization: from the amorphous precursor to crystalline $Yb:Lu_2O_3$. The weight loss associated with this interval is around 5%. Finally, stage E (950—1100 K) shows a weak exothermic peak at 1070.8 K, associated in previous literature with the growth of crystal particles [32]. From these results, the minimum calcination temperature must be higher than 950 K in order to convert the precursor oxide into crystalline $Yb:Lu_2O_3$.

To study the phase development as the calcination temperature and time increase, the precursor polymeric resin was calcined in air at different temperatures up to a maximum of 1023 K. Crystalline phase analysis was then carried out using X-Ray powder diffraction of the different products, as shown in Figure 3 for the synthesis of monoclinic KREW nanocrystals. In Figure 3a, the X-Ray powder diffraction pattern at 573 K corresponds to WO_3. At 723 K the peaks of the $KGd(WO_4)_2$(KGdW) monoclinic phase start to appear and the rest of the peaks correspond to a mixture of oxide compounds. This calcination temperature is therefore still too low to achieve complete crystallization of monoclinic KGdW. This approach gives an optimum calcination temperature of between 723 and 1003 K. Figure 3b shows X-Ray powder diffraction patterns for the calcination of $KYb(WO_4)_2$(KYbW) nanopowders. At 873 K, peaks from the KYbW monoclinic phase start to appear and some other peaks also indicate the presence of a mixture of unidentified oxide compounds. At around 923 K, the KREW X-Ray powder diffraction pattern corresponds exclusively to the monoclinic phase, and the shape of the peaks indicates a good degree of crystallization. We can see that the degree of crys-
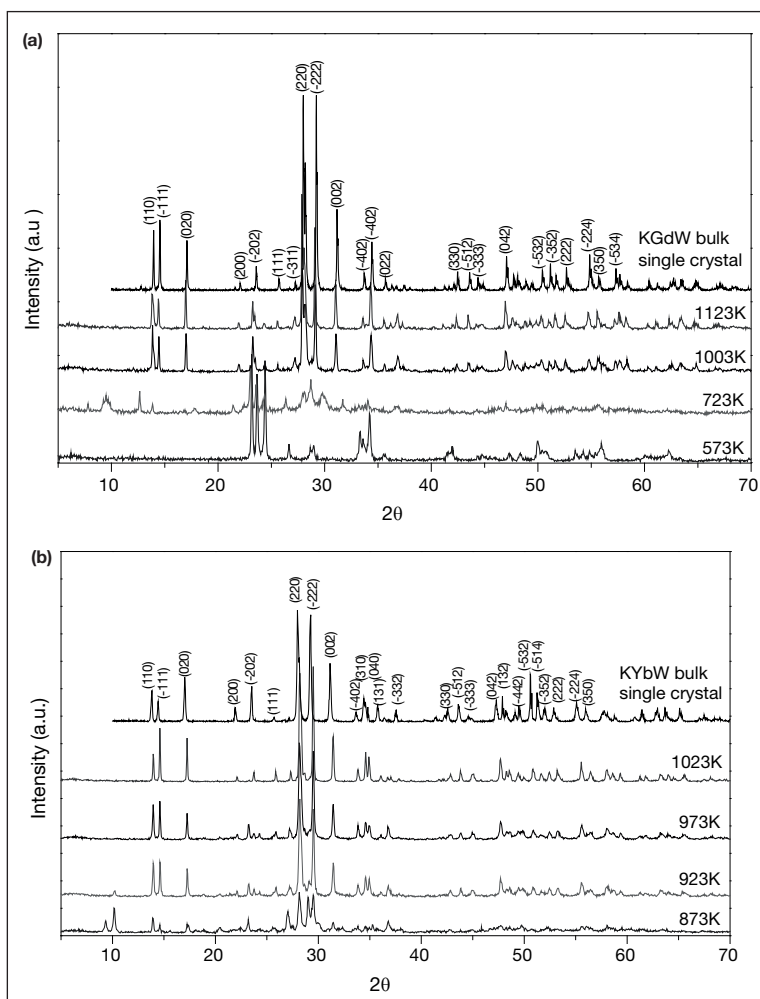

Figure 3. X-ray powder diffraction of the calcination procedure of precursor powder for **a)** KGdW **b)** KYbW.

tallization increases as the calcination temperature increases. However, an increase in calcination temperature also leads to an increase in the size of the nanoparticles. The optimum calcination temperature is therefore 973 K for synthesis of KREW nanocrystals. A similar study (reported in more detail in [33]) concludes that the optimum calcination temperature for preparing $Yb:Lu_2O_3$ nanocrystals is 973-1073 K.

The lattice parameters of the nanocrystals were calculated using the FULLPROF program [34] based on the Rietveld method [35]. Crystallite size, L, was measured using Scherrer's [36] equation $L = K\lambda/(\beta \cos\theta_B)$ for peak broadening from size effects only (β is the FWHM measured in radians on the 2θ scale, λ is the wavelength used, θ_B is the Bragg angle for the measured hkl peak and K is a constant equal to 0.9 for L taken as the volume-averaged crystallite dimension perpendicular to the hkl diffraction plane. The validity of the Scherrer formula has been widely discussed in the literature; it is only valid for particles < 500 nm.

Generally, the crystalline structure of the final nanopowder obtained by the modified Pechini method corresponded to the low-temperature phase of each compound system, which is the phase of interest for laser applications. This is important since KREW (RE = Gd and Yb) present polymorphism as a function of the temperature [37].

X-ray diffraction [XRD] patterns of the precursor powders at 673—1273 K and the data from JCPDS standard No. 43-1021[38] corresponding to the Lu_2O_3 single cubic crystal, are also shown in Figure 4. It can be observed that the final crystalline structure of the powder belongs to the cubic system, with the space group $Ia3$.

Refinement of the structure provided the unit cell parameters shown in Table 1. Oxides with smaller mean particle sizes usually have larger lattice parameters due to the creation of oxygen vacancies. For KREW nanocrystals, as the unit cell parameters were very similar to those of bulk single crystal samples (slightly smaller b; unit cell parameter) this effect was not observed. The crystal structure of cubic $Yb:Lu_2O_3$ was refined at room tem-
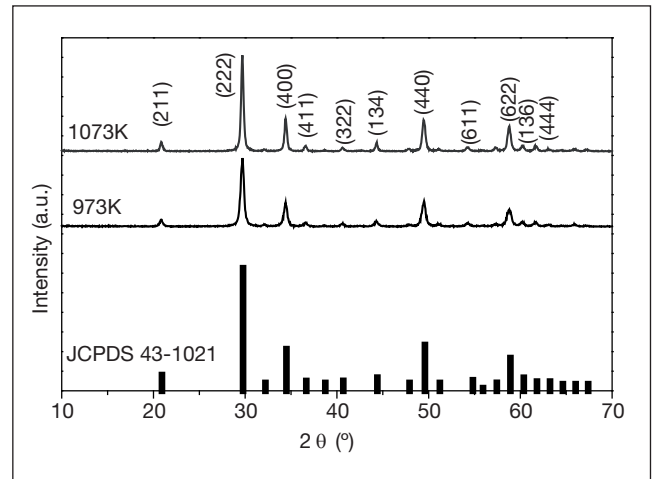

Figure 4. X-ray powder diffraction of $Yb:Lu_2O_3$ nanocrystals obtained by the calcination procedure at 973 K and at 1073 K.

perature using single crystal X-ray diffraction as the starting model. The refined unit cell parameter was a = 1.04136(3) nm, and Z = 16 for the space group $Ia3$. In this case, the increase observed in this unit cell parameter could be attributed to two overlapping effects: the introduction of ytterbium into the structure (cubic Yb_2O_3; unit cell parameter a = 1.043470 nm, JCPDS 41-1106) and the creation of oxygen vacancies.

Transmission electron microscopy was used with the microscope JEOL JEM-1011. Images were observed using a current accelerating voltage of 90 kV. It can be observed that some of the nanocrystals show a well-defined crystal habit. Figure 5a shows the habit of the KREW nanocrystals obtained by the modified Pechini method and the habit model of KGdW drawn using Shape software [39] based on a Wulff plot to index the observed (hkl) faces of the nanocrystals. The forms with the larger areas are {110}, {̄111} and {010}; forms {021} and {̄221} can also be seen, but are not well developed. The appearance of these forms is consistent with their large interplanar distance, d_{hkl}, and the PBCs parallel to them [40].

Table 1. Unit cell parameters of KREW, monoclinic system, space group $C2/c$, and $Yb:Lu_2O_3$, cubic system, space group $Ia3$

	a (Å)	b(Å)	c(Å)	β (°)	V	Grain size (nm)
KGdW bulk single crystal* [40]	10.652(4)	10.374(6)	7.582(2)	130.8(2)	634.2(5)	—
KGdW bulk crystal** [23]	10.6890(6)	10.4438(5)	7.6036(4)	130.771(3)	642.834	—
KGdW nanopowder**	10.6851(6)	10.4327(6)	7.5986(4)	130.770(3)	641.493(6)	90-100
KYbW bulk single crystal* [24]	10.590(4)	10.290(6)	7.478(2)	130.70(2)	617.8(5)	—
KYbW bulk crystal** [23]	10.6003(12)	10.2673(12)	7.5066(8)	130.766(6)	618.78(12)	—
KYbW nanopowder**	10.6026(6)	10.2597(6)	7.5036(4)	130.753(3)	618.33(6)	50-60

	a (nm)	Grain size (nm)
Lu_2O_3 bulk crystal *[29]	1.037	—
Lu_2O_3 bulk crystal **[38]	1.039	—
Yb_2O_3 bulk crystal** [1]	1.043470	—
$Yb:Lu_2O_3$ nanocrystal**	1.04136(3)	60

* By X-ray single crystal diffraction
** By X-ray powder diffraction
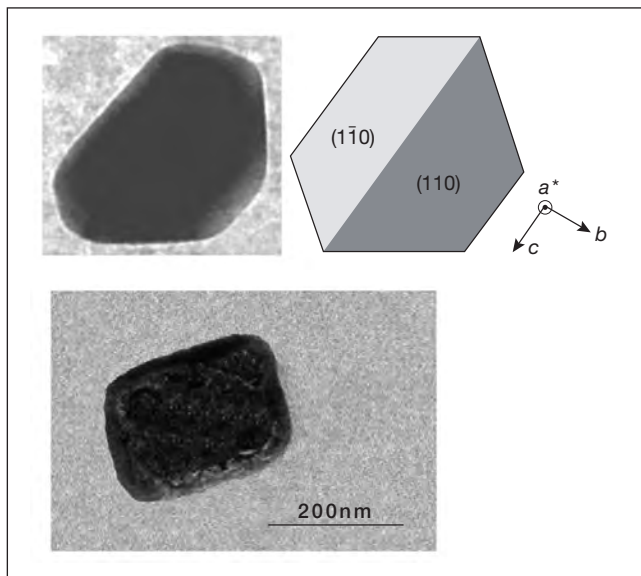
Figure 5. TEM micrographs of the crystal habit of a) KREW nanocrystals b) Yb:Lu$_2$O$_3$ nanoparticles.

Figure 5b shows the habit of a Yb:Lu$_2$O$_3$ nanocrystal obtained by the modified Pechini method. However, most of the particles have a rounded shape, due to their small size. For Yb:Lu$_2$O$_3$ nanocrystals, it was necessary to analyze the concentration of ytterbium in the nanocrystals. Using electron probe microanalysis (EPMA) we measured the composition of the nanocrystals as Yb$_{1.006}$Lu$_{0.994}$O$_3$ or (50 at.% Yb:Lu$_2$O$_3$).

Optical phonon confinement due to the small size of the nanocrystal grains may result in differences in the Raman spectra of the nanocrystals compared to those of bulk single crystals [41].

Figure 6 shows the Raman spectra for KREW nanocrystals at room temperature in the 0 to 1200 cm^{-1} frequency range, compared to the unpolarized Raman spectra of bulk KREW single crystals. The structures appearing at frequencies below 260 cm^{-1} can be attributed to external lattice modes; e. g., translational and rotational modes involving the heavy atoms of the unit cell. The ν2 and ν4 stretching modes appear in the 265-390 cm^{-1} region and the ν1 and ν3 bending modes in the 800-1100 cm^{-1} region. The bands in the 370-800 cm^{-1} region are related to double oxygen bridge vibrations activated when the coordination number of tungsten is increased from 4 to 6. The large cross section of the three peaks located at 86, 759 and 903 cm^{-1} for KGdW and 87, 758 and 908 cm^{-1} for KYbW makes KREW nanocrystals attractive for SRS applications. The Raman gain coefficient is linearly proportional to the scattering cross section and inversely proportional to the linewidth of the spontaneous Raman line [42]. Table 2 shows the linewidths, *Δν,* of the three main KREW nanocrystal peaks. Compared to the Raman spectra of the bulk single crystals, the nanocrystal peaks with higher phonon energies have larger linewidths and those with lower phonon energies have narrower linewidths. We can see that the peak around 87 cm^{-1} has a promisingly narrow linewidth compared to those reported in the literature for YAG ceramics
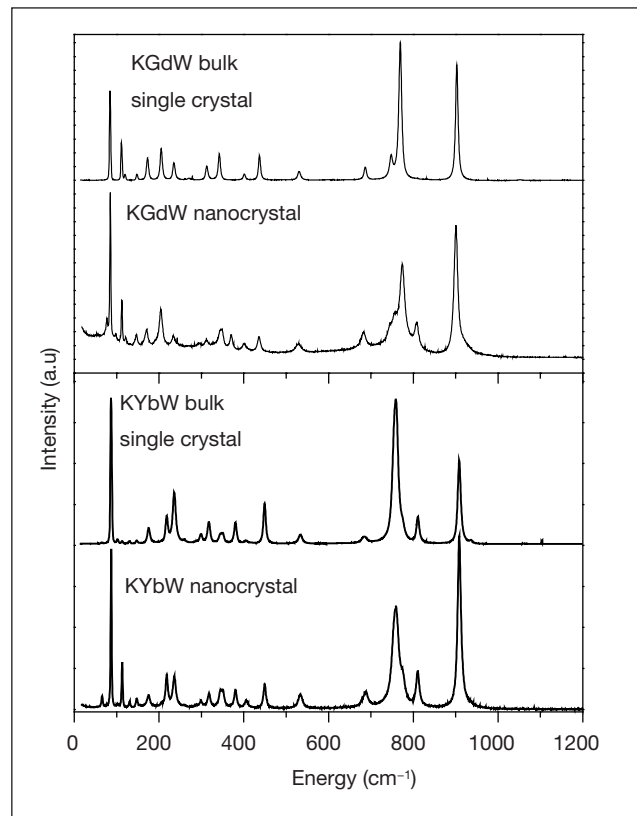

Figure 6. Raman spectroscopy of KGdW and KYbW nanocrystals and their bulk counterparts.

(5.7 cm^{-1}) and sesquioxide ceramics (Y$_2$O$_3$ = 4 cm^{-1} and Sc$_2$O$_3$ = 3.7 cm^{-1}) [42].

Table 2. Vibrational frequencies and linewidths of the spontaneous Raman peaks of KREW

KGdW nanocrystal		KGdW bulk single crystal	
Phonon energy (cm^{-1})	Δν (cm^{-1})	Phonon energy (cm^{-1})	Δν (cm^{-1})
86	2.4	84	3.0
772	12.5	769	7.0
903	8.7	902	6.54
KYbW nanocrystal		KYbW bulk single crystal	
Phonon energy (cm^{-1})	Δν (cm^{-1})	Phonon energy (cm^{-1})	Δν (cm^{-1})
87	2.5	90	3.8
758	18.2	763	14.6
908	9.13	911	8.4

To examine the distribution of size and the homogeneity of the nanocrystals we observed them under a JEOL JSM 6400 scanning electron microscope (SEM) and a JEOL JEM-1011 transmission electron microscope (TEM). Figure 7 shows the SEM images of the Yb:Lu$_2$O$_3$ nanocrystals obtained by calcination for 1-3 h at 1073 K. They indicate: when calcination at 1073 K increases from 1 to 2 h, the size of the nanocrystals also increases; and when the calcination time reaches 3 h, a kind of sintering process takes place and the nanocrystals tend to form more aggregates. So, more homogeneous nanocrys-
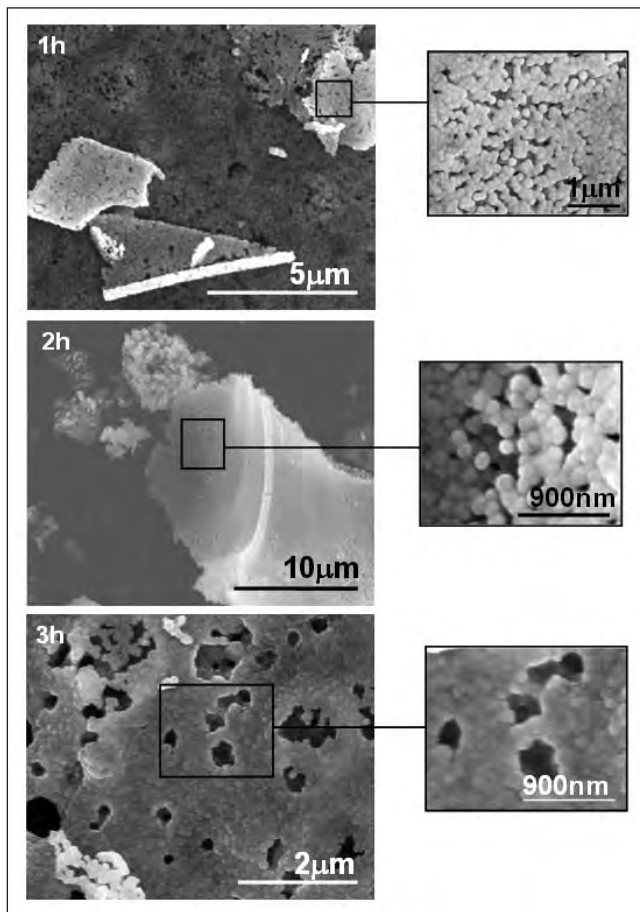
Figure 7. SEM images of the Yb:Lu$_2$O$_3$ nanocrystals after calcination at 1073 K for 1, 2 and 3 h.

Figure 9. Absorption and emission spectra of Yb:Lu2O3 nanoparticles at room temperature. The nanoparticles were synthesized at 1073 K over 2 h.

tals of around 100 nm can be obtained by calcination at 1073 K for 1-2 h.

Figure 8 shows TEM images of the KGdW nanocrystals (CM = 3, CE = 2) and KYbW (CM = 1, CE = 2) nanoparticles obtained by calcination at 973 K. We analyzed the effects of different CM and CE ratios. CM = 1 and CE = 2 led to smaller and more homogeneous particles. However, CE did not significantly influence the final size of the KREW and Yb:Lu$_2$O$_3$ particles.

We measured room- and low-temperature optical emission and optical absorption spectra using a Cary Varian 500 Spectrophotometer. To work at low temperatures we used an Oxford cryostat with helium-gas f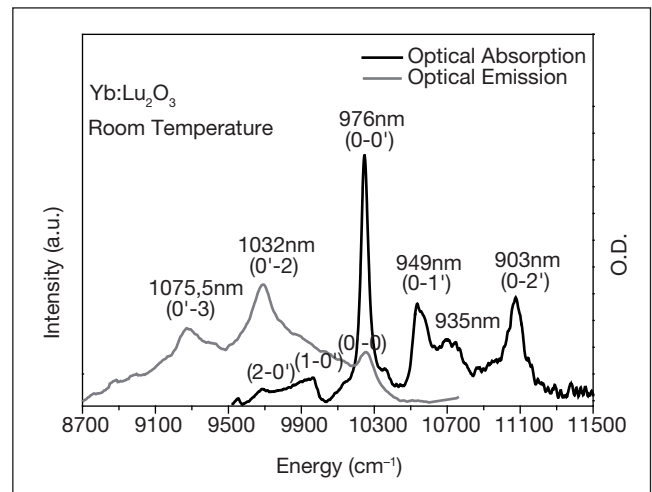low. Fluorescence, collected at 90°, was dispersed by a 0.46 m double monochromator (JOBIN YVON- SPEX HR 460) and by a cooled Hamamatsu R55092-72 NIR photomultiplier in the NIR range. A Ti:sapphire laser at 903 nm was used to excite the nanocrystals. As mentioned above, Lu$_2$O$_3$ forms a cubic crystalline system with space group $Ia3$. This type of structure has two cation sites available for Lu^{3+} and Yb^{3+}; one with C$_2$ symmetry and the other with C3i($\bar{3}$) symmetry. The ratio of C$_2$ to C$_{3i}$ is 3:1, that is, of the 32 cations present in the structure, 24 are distributed in C$_2$ sites and 8 in C$_{3i}$ sites. There is no preference for occupation of these two sites by the rare earth doping ions [29]. Figure 9 shows the room-temperature optical (875-1050 nm wavelength) absorption of Lu$_2$O$_3$ nanocrystals doped with 50% ytterbium. The absorption spectrum presents four absorption peaks at 903, 935, 949, and the strongest and sharpest at 976 nm. This manifold is associated with the ytterbium transition $^2F_{7/2} \rightarrow {}^2F_{5/2}$. This room-temperature absorption pattern is very similar to that of the corresponding bulk counterpart [43]. Figure 10 shows the emission spectrum at room temperature associated with the $^2F_{5/2} \rightarrow {}^2F_{7/2}$ transition, after excitation at 903 nm, corresponding to the $^2F_{7/2}(0) \rightarrow {}^2F_{5/2}(2)$ transition for Yb^{3+} located at the C$_2$ symmetry site [41].

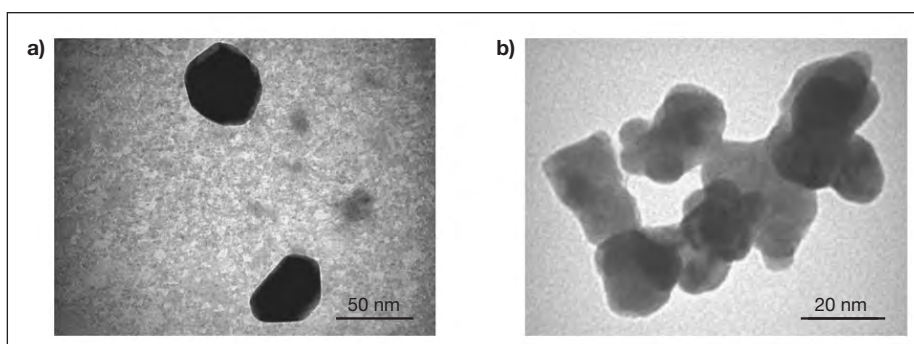Optical absorption and emission at low temperature (6 K) was performed to determine the Stark sublevels of the excited

Figure 8. TEM photographs of (a) KGdW (C_M = 3, C_E = 2, T = 973 K) and (b) KYbW (C_M = 1, C_E = 2, T = 973 K) nanoparticles.

$^2F_{5/2}$ state. The absorption bands at low temperature are slightly sharper than at room temperature, but they still appear broader than those of their bulk counterpart [44]. The broadening of spectral lines could indicate disorder in the local environment of the absorbing ion. This disorder could be a lack of structural order throughout the particles, or a lack of order due to oxygen vacancies, or surface disorder [45]. The Stark sublevel energy values for ytterbium in bulk Lu_2O_3 are reported in the literature [46] [47]. Table 3 summarizes the energy values obtained for Yb:Lu_2O_3 nanocrystals.

Table 3. Energy levels of trivalent ytterbium in Yb:Lu_2O_3 nanocrystals

		Yb:Lu_2O_3 bulk single crystal [29] (cm^{-1})	Yb:Lu_2O_3 nanocrystal (in this work) (cm^{-1})
$^2F_{5/2}$	(2')	11073	11074
	(1')	10666	10539
	(0')	10244	10246
$^2F_{7/2}$	(3)	903	947
	(2)	514	556
	(1)	427	----
	(0)	0	0

3. Wide-bandgap semiconductor sub-micronsized structures doped with lanthanide ions

The photoemission generated by lanthanide (Ln) ions when introduced into semiconductors is limited by the low solubility of Ln in semiconductors, and severe temperature quenching at room temperature [7]. However, this thermal quenching decreases as the bandgap of the semiconductor increases [8]. So, wide-bandgap semiconductors are more attractive hosts for Ln ions. Among them, gallium nitride (GaN)—with important applications in the production of UV and blue light emitters, and of optoelectronic high-power/high-temperature devices [6]—is of particular interest as an Ln ion host. Its direct bandgap may allow electrical excitation of Ln ions through the impact of hot carriers with the Ln ions, or as a result of nearby electron-hole recombination. These mechanisms can generate a near-ideal optical emission, which can be properly amplified [9].

Among the different optical emissions generated by Ln ions, the 1.5-μm emission generated by erbium (Er) is of particular interest for optical communications. This has made this ion the main Ln doping ion studied in semiconductors [48], [49].

One-dimensional GaN nanostructures (nanowires, nanorods and nanotubes) are expected to enhance the quantum efficiency of light generation in these semiconductors more than any other [50] [51]. Incorporating Er into these one-dimensional GaN structures may produce new functional devices through hybridization with a variety of other passive and active optical materials. Furthermore, Ln-doped nanorods or nanowires grown on Si (001) substrates may produce light sources operating at wavelengths throughout the visible and near-infrared range that are built directly on Si substrates without any post-growth process. The integration of electronic and

photonic systems on a single Si substrate may also result in the development of on-chip optoelectronic devices.

Using catalyst-assisted chemical vapor deposition (CVD) we successfully synthesized Er-doped GaN sub-micronsized rods on silicon (001) substrates for the first time [52]. The synthesis was performed in a horizontal tubular furnace using gallium metal (99.99999%), ammonia (99.999%), and erbium metal (99.9%, 325 mesh) together with silicon (001) substrates covered with nickel, as the catalyst. The quartz tube of the furnace was degassed to a vacuum pressure of 1 × 10^{-2} Torr, and then ammonia gas was introduced at a flow rate ranging from 50 to 75 sccm. In all the experiments the total pressure at the downstream end of the furnace was kept at 15 Torr using no additional carrier gas (only ammonia). Upon heating to a preset temperature between 1073 and 1173 K, the reaction proceeded for 1 hour, after which time the flow of NH$_3$ was stopped and the system was cooled to room temperature.

SEM images of the sub-micron-sized Er-doped GaN rods obtained are shown in Figure 10. The rods have a hexagonal cross section with diameters ranging between 500 and 950 nm, and lengths of up to 10 mm. The hexagonal cross section is a clear indication that the rods are wurtzite GaN growing along the **c** crystallographic direction. Pyramidal tips less than 100 nm in diameter are observed at the end of the rods. No precipitates were observed on the surface of the rods and the SEM images reveal no layers with a different contrast, which suggests that the Er has been incorporated into the GaN structure. The presence of some Ni-based clusters at the end of the rods (as determined by energy-dispersive X-ray analysis) suggested that the growth of these rods proceeded via a vapor-liquid-solid mechanism (VLS) [52]. This means that the semiconducting material or its precursors, including Er, in vapor form were incorporated into the growing rods by means of a droplet of liquid catalyst. These droplets, located at the tips of the rods, acted as seeds for the growth, thus determining the wires' diameters.
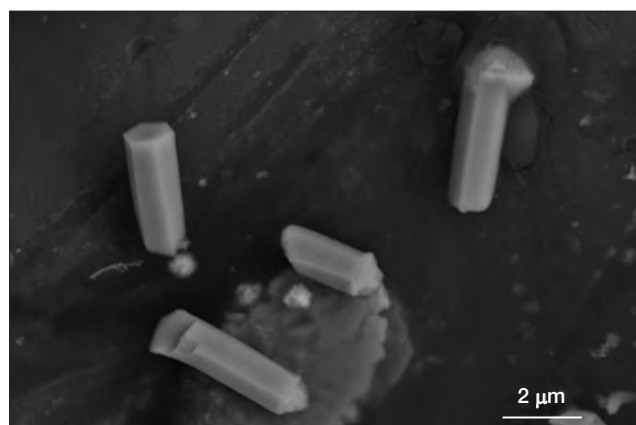

Figure 10. Scanning electron micrograph showing several Er-doped GaN sub-micron-sized rods synthesized on a Si (001) substrate. The hexagonal cross section of the rods is typical of wurtzite GaN growing along the c crystallographic direction. The rods have diameters of approximately 900 nm, with lengths of up to 10 μm. Some of them show pyramidal tips with diameters of less than 100 nm. Some Ni-based clusters are observed at the ends of some of the rods.
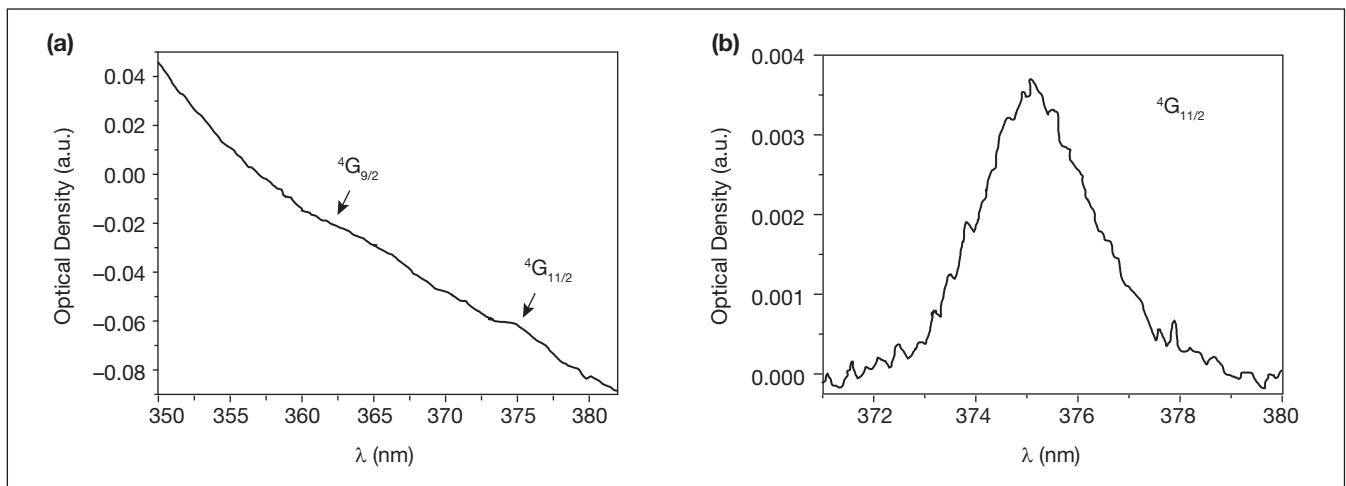
Figure 11. (a) Optical absorption spectrum of Er-doped GaN sub-micron-sized rods in the range 350-383 nm, showing the $^4G_{9/2}$ and $^4G_{11/2}$ optical absorption manifolds of Er. (b) Magnification of the previous absorption spectrum showing the $^4G_{11/2}$ manifold in detail.

We have identified several Er optical absorption bands in the rods at room temperature, including the hypersensitive bands. To measure the frequencies, the rods were dispersed in ethanol and homogenized with ultrasound inside a quartz cell. The sample was then introduced into the sample chamber of a Varian Cary 500 Scan spectrophotometer. Figure 11 shows the optical absorption spectrum of Er-doped GaN rods near the bandgap of the semiconductor. Two small peaks in this spectrum indicate the presence of the $^4G_{9/2}$ and $^4G_{11/2}$ optical absorption manifolds of Er. Due to the low number of Er-doped GaN rods dispersed in ethanol, the intensity of the absorption bands was extremely low. This made it impossible to resolve the fine structure expected in these bands. However, the position of the manifolds at 362 and 375 nm leaves no doubt as to the origin of these bands which could only be caused by Er in the rods [53]. The identification of these bands might make it possible to enhance the quantum yields of the emissions corresponding to Er by carefully designing the host environment. The bandgap of the semiconductor would need to be tailored via an appropriate solid solution in the GaN, InN, and AlN system, to fit perfectly with the target Er absorption band. This strategy could overcome the problems in the application of Er-doped GaN thin-films and nanostructures caused by the poor quantum yield at the characteristic wavelengths of the bound-exciton radiation (at around 358 nm) as well as at wavelengths generated by Er in the IR region (at around 1.54 µm) when stimulated electrically [54]. This approach is not only valid for Er but could also be extended to the rest of the Ln ions embedded in III-nitride semiconductors.

Additional evidence for the incorporation of Er in the GaN rods was provided by confocal microscopy using a Nikon Eclipse TE 2000-E confocal microscope after excitation at 488, 543 and 633 nm. Figure 12 shows an image of an Er-doped GaN sub-micron-sized rod attached to a GaN-catalyst alloy particle under excitation at 488 nm. Both the Er-doped GaN rod and the catalyst cluster containing Er show emission in the 495-540 nm and the 640-900 nm regions. However, no emission was observed in the 560-610 region. When the Er-doped GaN rods were excited at 543 nm, emission was only observed

in the 640-900 nm region. No emission was observed when pumping at 633 nm.

The observation of emissions coming from these Er-doped GaN rods in different regions depending on the excitation energy used can be explained as follows. Pumping at 488 nm excites the Er through the absorption of light by the $^4F_{7/2}$ manifold [53]. From this excitation level, the system can relax nonradiatively to the $^2H_{11/2}$ manifold, from which emission can be produced at 537 nm when the system relaxes radiatively to the ground state ($^4I_{15/2}$) [49]. The emission detected in the 640-900 nm region corresponds to the $^4F_{9/2} \rightarrow {}^4I_{15/2}$ transition observed in the range between 655 and 675 nm in other matrices [55]. The transitions involved in all these processes are summarized in Figure 13. Excitation at 543 nm stimulates Er through the absorption of light by the $^4S_{3/2}$ manifold. The fact that emission is only observed in the 640-900 nm region indicates that the system relaxes non-radiatively from this level to the $^4F_{9/2}$ manifold, from which it can emit in the red range through the $^4F_{9/2} \rightarrow {}^4I_{15/2}$ transition. Finally, the fact that no emission is observed
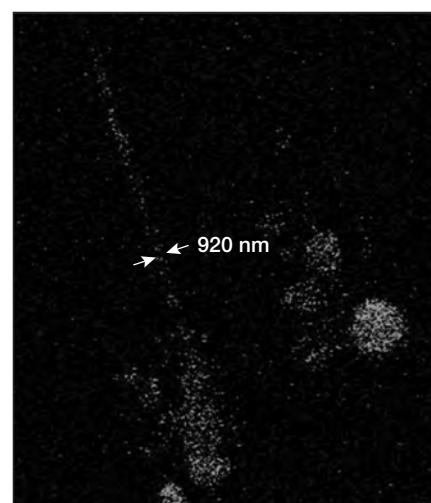

Figure 12. Confocal microscope image of an Er-doped GaN sub-micron-sized rod attached to a catalyst-cluster emitting in the 495-540 nm range after excitation at 488 nm.
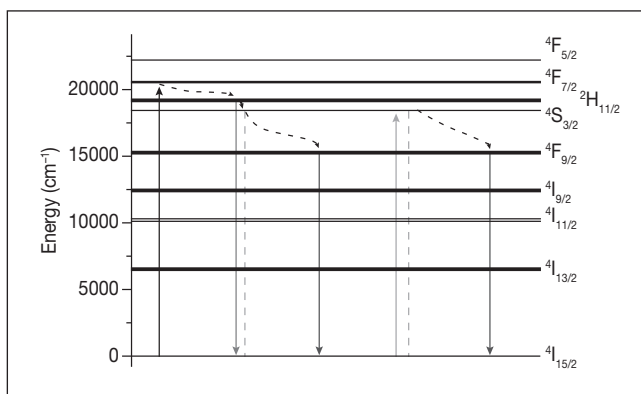
Figure 13. Schematic diagram of electronic energy levels of Er showing the transitions involved in the absorption and emission of light in the Er-doped GaN sub-micron-sized rods.
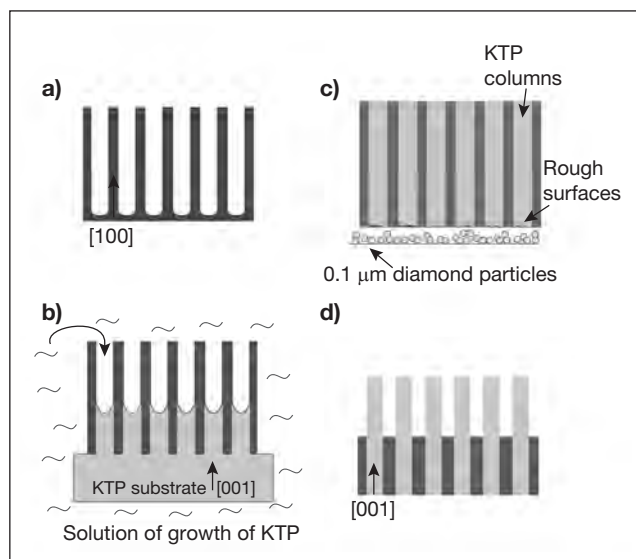

Figure 14. Schematic view of the four stages of growth of KTP 2D PCs. a) Preparation of the oriented 2D macroporous silicon membrane. b) The silicon template is attached to an oriented KTP substrate and then immersed in the growth solution of KTP. c) After growth, the top of the columns is polished with diamond particles in order to obtain an optical-quality surface. d) Silicon is partially removed by selective chemical etching.

when excited at 633 nm, also constitutes evidence of the presence of Er in the rods, as no Er absorption bands can be found at these wavelengths. Therefore, the system cannot be stimulated and no emission is observed. Although other Er emissions may be expected in the near infrared (around 1.5 microns) they were not recorded due to the limitations of our detection system.

Although Er has been incorporated into other ErSi$_{2-x}$ [56], Si [57] and ZnO [58] nanowires, this is the first time, to the best of our knowledge, that visible emission has been reported from such one-dimensional structures. Of special importance is the observation of green and red emissions coming from Er in these rods obtained by directly pumping Er at energies below the bandgap of the semiconductor at room temperature. Such Ln-doped GaN one-dimensional structures may be used to produce cost-efficient full-color displays, with the possibility of taking advantage of the anisotropic properties of GaN. This has implications for the polarization of the light emitted, by controlling the growth direction of the Er-doped GaN rods. In the future, through doping and co-doping with multiple Ln ions, the emission spectrum can be further customized and the perceived color varied over a very wide range. This is further evidence of the versatility of the approach based on the incorporation of lanthanide ions in III-nitrides which is not feasible with semiconductor alloys alone.

4. Arrays of one-dimensional structures of non-linear optical materials as photonic crystals

If we can create arrays of micro- and nanowires of non-linear optical materials, we will be able to produce structures that act as PCs. Although this approach is not restricted to non-linear optical materials, PCs are an ideal framework in which to control optical non-linear interactions, as they may enhance [10] [11] [12], phase match [13] [14], or cause a non-vanishing second-order interaction with a beam of light even if the material is centrosymmetric [15]. For instance, the structure of the dielectric material together with the modulation of the second-order non-linear susceptibility may lead to a backward parametric oscillation [16]; a non-linear effect predicted many years ago

but still unproven experimentally. Among all the possible PC structures, 2D photonic structures are, perhaps, the most interesting, as such structures can be easily integrated into optoelectronic devices meant for light amplification, light generation at altered frequencies, optical-data processing, or any kind of sensing [17] [18][19] [20].

We developed a new procedure that patterns inorganic crystals more efficiently, and which may facilitate the production of new light modulators that could take full advantage of the non-linear optic and electroptic coefficients of such materials [59]. Our approach is especially interesting as it constitutes a viable and cost-effective method of integrating non-linear optic materials into silicon-based devices. Until now, inorganic non-linear optical materials, such as KTiOPO$_4$ (KTP) or LiNbO$_3$, have been patterned by periodic poling followed by selective domain etching to obtain 1D arrays with a sub-micrometer spacing [60][61]. However, it is still difficult to accurately control the size of small domains. Moreover, after poling, one ends up with a stand-alone sample that would certainly be difficult to embed in any silicon-based device. We developed a completely novel combination of both top-down and bottom-up approaches to grow 2D PCs of KTP. These crystals are grown in 2D ordered macroporous silicon templates, so that the silicon matrix and the structured non-linear material, which will eventually be used to modulate or generate light, forms an integrated unit.

The procedure can be summarized by four different steps: the preparation of a high-quality ordered macroporous silicon template; the growth of KTP wires in the silicon template following the crystalline orientation of a KTP substrate closely bound to the silicon template; the polishing of the top or bottom surface of the KTP ordered structure; and finally, a partial selective etching of the silicon matrix. The sequence of these four steps is shown schematically in Figure 14.
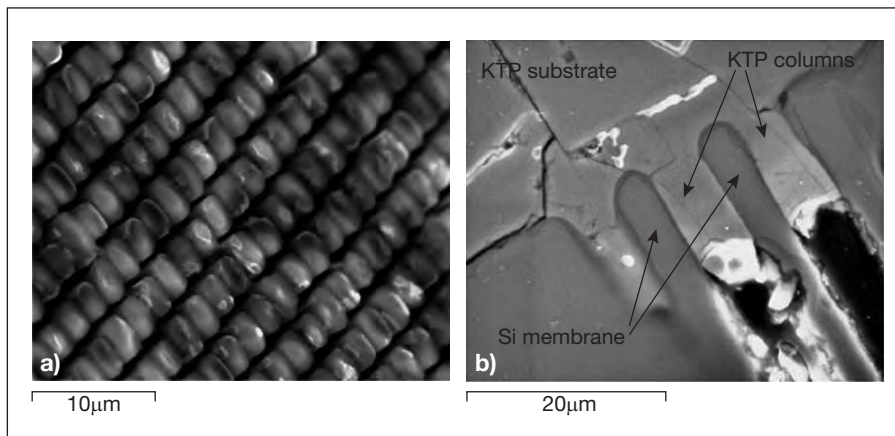
Figure 15. a) SEM image of the final 2D photonic crystal formed of an array of independent KTP wires, after polishing of the surface of the wires and selective etching of the Si template. b) Backscattered electron image of the initial stages of growth of the KTP wires inside the Si template coming from the top of the KTP substrate.

The silicon membranes were prepared by light-assisted electrochemical etching of n-type (100) silicon [62] and postprocessing. The front of the wafers was patterned with inverted pyramid-shaped pits, with a square base arranged in a square periodic lattice, by oxidation, photolithography, and subsequent tetramethyl ammonium hydroxide (TMAH) etching. An indium tin oxide (ITO) film was sputtered on the back of the silicon wafer to provide a low-resistance transparent ohmic contact. The wafers (as working electrodes) were incorporated into an electrochemical etching cell containing a 2.5 wt% aqueous solution of HF acid, and illuminated with a 100 W halogen lamp. The quality and size of the pores was controlled by a computerized feedback mechanism that regulated the generation of holes by continuously adjusting the back-illumination to maintain a constant current. After pore growth, the ITO layer was removed and the back of the wafer polished down until the holes opened, thereby obtaining a free-standing silicon template.

In the second step, the silicon template was bound to a single KTP crystal plate using a platinum wire. The KTP crystal was extremely accurately oriented so the largest surface was perpendicular to the *c* crystallographic direction with the edges parallel to the *a* and *b* crystallographic directions. The template/substrate ensemble was dipped for 5 min into the high-temperature KTP growth solution, where a degree of supersaturation of about 2% had been created, without any additional thermal gradient. Then, the template/substrate/epitaxy composite was removed from the solution while the furnace was cooled to room temperature at a cooling rate of 15 Kh^{-1} to avoid thermal stresses that could crack either the 2D photonic structures or the substrate.

After growth, the top part of the KTP wires was mechanically polished. However, due to the different degrees of hardness of silicon and KTP, it was not easy to polish both materials at the same time to obtain an optical-quality top surface. The best results were obtained using diamond powders with a particle size of 0.1 μm.

The last step was to remove the silicon template by selective chemical etching with TMAH diluted in distilled water (5 vol%) at 354 K.

Figure 15a shows that the final 2D PC is formed of an array of independent KTP wires. When using a 100-μm-thick silicon template and after the full process to obtain optical-quality sam-

ples was completed, the estimated lengths of the wires were 70-80 μm, with resulting aspect ratios (height/diameter) of up to 28-32. We were able to produce PCs with lattice parameters ranging from 4.5 to 10 μm. However, from the data collected from the growth procedure we followed there is nothing to indicate that 2D KTP PCs with smaller diameter wires could not be grown, as macroporous silicon templates with a smaller diameter pore, or alternatively, anodized alumina templates with pore diameters between 20 to 200 nm, are readily available. The chemical composition of the columns was measured using energy-dispersive X-ray analysis. We concluded that the columns were formed exclusively of KTP. In Figure 15b, one can clearly see that the KTP columns grow from the substrate, whereas the silicon mask acts as a template for the growth.

The crystallographic orientation of the 2D photonic structure of KTP was compared to the crystallographic orientation of the original KTP substrate by X-ray texture analysis. This procedure also provided an estimate of the degree of crystallinity of the columns and the orientation of the wires relative to the crystallographic axes, as is shown in Figure 16. Figure 16-left shows the 2θ scan for the KTP PC (pattern i) and the substrate (pattern ii). The peak with the highest intensity in these patterns is the (004) peak, with full width at half maximum values (FWHM) similar for the photonic structure and the initial substrate (0.4°). This indicates a high degree of crystallinity of the photonic structure. The (004) and (204) pole figures in Figure 16-right corresponding to the 2D KTP wire arrangement confirm the high degree of orientation of the axis of the KTP wires parallel to the *c* crystallographic direction. The X-ray powder diffraction pattern obtained for a KTP crystalline powder sample, milled from a single crystal, is also shown in Figure 16 (pattern iii) to compare the degree of texturization of the columnar sample. The reflections were indexed according to the powder diffraction pattern of KTP [63]. In this diffraction pattern, the peak with the maximum intensity was not that corresponding to the (004) plane (as observed in the other diffraction patterns) which indicated, again, the high degree of texturization and orientation of the KTP wires.

To demonstrate the PC properties of the 2D structures, we measured the specular reflection as a function of the wavelength of the incident field in a 2D PC with a square lattice array of KTP wires in air with a 4.5 μm periodicity//4.5 μm spacing in the XΓ direction. A dip in this reflection spectrum should be
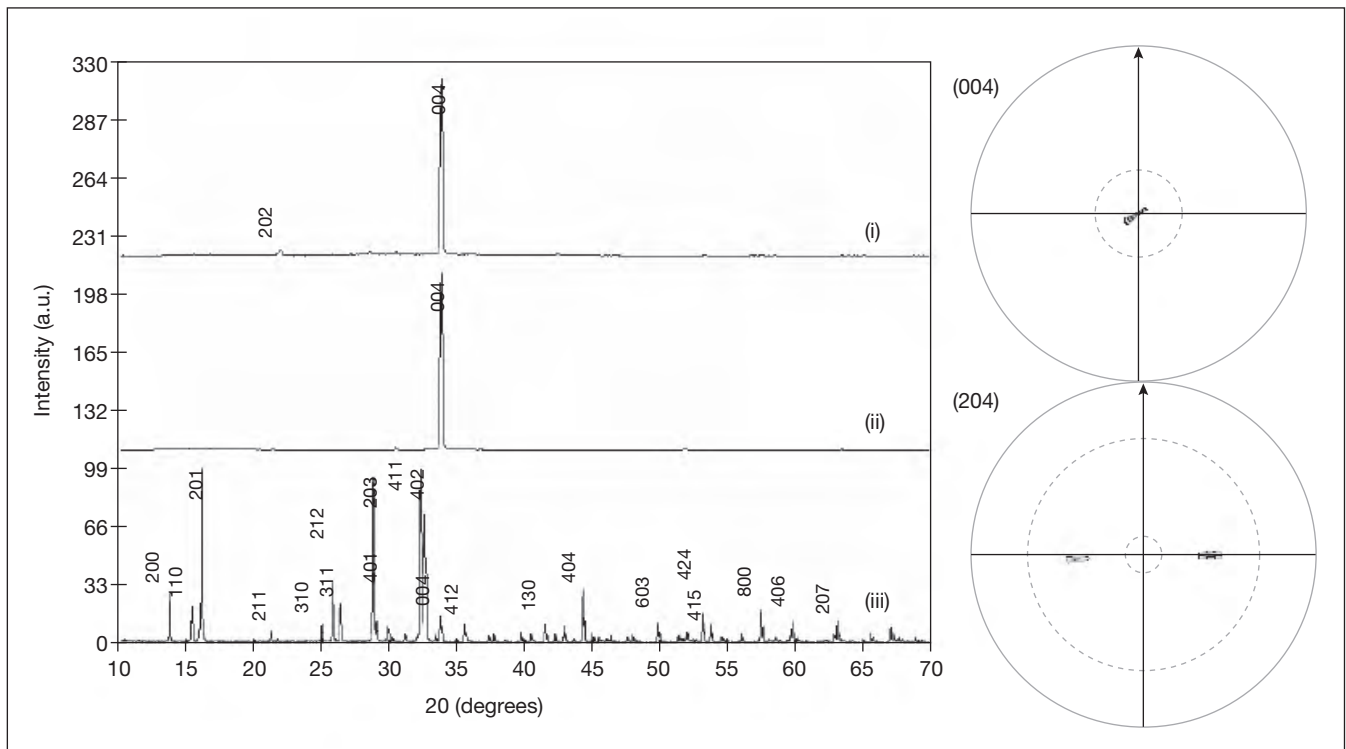
Figure 16. Left: X-ray texture analysis: i) 2θ scan for the photonic structure, ii) 2θ scan for the substrate, and iii) 2θ scan for KTP crystalline powders. Right: (004) and (204) pole figures corresponding to the 2D KTP PC.

found when the wavevector component of the transmitted field, which lies on the plane that separates the top of the KTP columns from the air, couples to any one of the forbidden bands of the 2D band structure [64]. The wavelength of the incident light, fixed at an angle of 25° with respect to the axes of the columns, was tuned in the spectral range of 940—1220 nm. The reflected light was detected using a pyroelectric detector with a flat response in the same range. A dip in specular reflectance was found when the incident light was tuned at 1100 nm. The spectral position of the dip coincides with the spectral position of the third-order Bragg reflection band determined from a numerical calculation of the transmission in the X-direction using the transfer matrix formalism [65] [66]. The 2D pattern of the KTP wire array is also apparent from the diffraction of reflected light, since the surface of the 2D PC of KTP acts as a 2D diffraction grating, as is shown when it is illuminated with the SH at 527 nm of the linearly polarized 1 ps laser pulses at 1055 nm. An extended discussion of these results can be found in [67].

From these results it is clear that the procedure presented fully controls the crystalline direction of growth with respect to the direction of the wires of the 2D arrangement. This is important since one may use the most appropriate non-linear or electrooptic coefficient in combination with a phase-matching condition, which would be provided by the 2D photonic structure. This is not possible with bulk KTP, where phase matching relies on the birefringence and the coefficients with the largest non-linearity cannot be used for efficient SH generation. As mentioned above, this procedure is not restricted to the wire diameters grown here; it can be extended to wire arrays with smaller diameters as soon as high-quality porous templates,

made from silicon or alumina, become available. Also, 3D photonic structures can be produced if appropriate templates are available. Progress is currently being made in this direction. These structures may facilitate the generation of light at higher frequencies, the electrooptic modulation of light, or backward parametric amplification and oscillation, and should be very easily integrated into silicon-based devices.

Acknowledgements

References

[1]   Gleiter H. (1989). *Prog. Mater. Sci*. 33:223
[2]   Tissue B.M., Bihari B. (1998). *J. Fluoresc*. 8:289

[3] Meltzer R.S., Feofilov S.P., Tissue B., Yuan H.B. (1998). *Phys. Rev. B*. 60:R14012

[4] Dong J., Shirakawa A., Ueda K., Yagi H., Yanagitani T., Kaminskii A.A. (2007). *Optics Lett*. 32:1890

[5] Reisfeld R., Jorgensen C.K. (1992). *Structure and Bonding*. Springer-Verlag: Heidelberg

[6] Gil B. (1998). *Group III nitride semiconductor compounds*. Oxford Science Publications: Oxford; Nakamura S., Pearton S., Fasol G. (2000). *The Blue Laser Diode*. 2nd. Ed., Springer-Verlag: Berlin

[7] Zavada J.M., Zhang D. (1985). *Solid State Electron* 38:1285

[8] Favennec P.N., L'Haridon H., Salvi M., Moutonnet D., Guillou Y.L. (1989). *Electron. Lett.* 25:718

[9] Steckl A.J., Heikenfeld J.C., Lee D.S., Garter M.J., Baker C.C., Wang Y. (2002). *IEEE J. Selected Topics in Quantum Electron.* 8:749

[10] Trull J., Vilaseca R., Martorell J., Corbalan R. (1995). *Opt. Lett.* 20:1746

[11] Markowicz P.P., Tiryaki H., Pudavar H., Prasad P.N., Lepeshkin N., Boyd R.W. (2004). *Phys. Rev. Lett.* 92:083 903

[12] Torres J., Le Vassoi d'Yerville M., Coquillat D., Centeno E., Albert J.P. (2005). *Phys. Rev. B: Condens. Matter Mater. Phys.* 71:195 326

[13] Martorell J., Vilaseca R., Corbalan R. (1997). *Appl. Phys. Lett.* 70:702

[14] Centini M., Sibilia C., Scalora M., D'Aguanno G., Bertolotti M., Bloemer M.J., Bowden C.M., Nefedov I. (1999). *Phys. Rev. E: Stat., Nonlinear, Soft Matter Phys.* 60:4891

[15] Martorell J., Vilaseca R., Corbalan R. (1997). *Phys. Rev. A: At., Mol., Opt. Phys.* 55:4520

[16] Martorell J. (2005). *Appl. Phys. Lett.* 86:241 113

[17] Noda S., Imada M., Okano M., Ogawa S., Mochizuki M., Chutinan A. (2002). *IEEE J. Quantum Electron* 38:726

[18] François M., Danglot J., Grimbert B., Mounaix P., Muller M., Vanbésien O., Lippens D. (2002). *Microelectron. Eng.* 61—62:537

[19] Malvezzi A.M., Cattaneo F., Vecchi G., Falasconi M., Guizzetti G., Andreani L.C., Romanato F., Businaro L., Di Fabrizio E., Passaseo A., Di Vittorio M. (2002). *J. Opt. Soc. Am. B* 19:2122

[20] Vecchi G., Torres J., Coquillat D., Le Vassor d'Yerville M., Malvezzi A.M. (2004). *Appl. Phys. Lett.* 84:1245

[21] Sole R., Nikolov V., Ruiz X., Gavalda Jna., Solans X., Aguilo M., Diaz F. (1996). *J. Cryst. Growth* 169:600

[22] Pujol M.C., Solé R., Gavaldà Jna., Massons J., Aguiló M., Díaz F. (1999). *J. Mater. Research* 14:3739

[23] Pujol M.C., Mateos X., Solé R., Massons J., Gavaldà Jna., Díaz F., Aguiló M. (2001). *Mater. Sci Forum* 710:378

[24] Pujol M.C., Solé R., Massons J., Gavaldà Jna., Solans X., Díaz F., Aguiló M. (2002*). J Appl Crystallogr* 35:108

[25] Petrov V., Pujol M.C., Mateos X., Silvestre O., Rivier S., Aguiló M., Solé R.M., Liu J., Griebner U., Díaz F. (2007). *Laser & Photon. Rev*. 1:179

[26] Morrison C.A., Leavitt R.P. (1982). In: K.A. Gschnieder, L. Eyring (Eds.), Handbook on the Physics and chemistry of Rare Earths, New York.

[27] Mix E., Fornasesiero L., Diening A., Petermann K., Huber G. (1998). *Adv. Sol. State Lasers*, *OSA TOPS* 19:122

[28] Klein P.H., Croft W.J. (1967). *Appl. Phys*. 38:1603

[29] Pauling L., Shapell M.D. (1930). *Z. Kristallagr*. 75:128

[30] Galceran M., Pujol M.C., Aguiló M., Díaz F. (2007). *J. Sol-gel Science and technology* 42:79

[31] Interranta L.V., Jiang Z., Larkin D.J. (1998). *ACS Symposium Series 77*:168

[32] Guo H., Yin M., Dong N., Xu M., Lou L., Zhang W. (2005). *Appl. Surf. Sci*. 243:245

[33] Galceran M., Pujol M.C., Aguiló M., Díaz, F. (2007). *Materials Science and Engineering B*, in press.

[34] Rodriguez-Carvajal J. (2000). Reference guide for the computer program Fullprof. Laboratorie León Brillouin. CEA-CNRS. Saclay, France.

[35] Rietveld H.M. (1969). *J. Appl. Cryst.* 2:65

[36] Cullity B.D. (1978). Element of X-Ray Diffraction, Addison-Wesley.

[37] Klevtsov P.V., Kozeeva L.P., Kharchenko L.Y., Pavlyuk A.A. (1974). *Sov. Phys. Crystallogr*. 19:342

[38] Grier D., McCarthy G. (1991). North Dakota State University, Fargo, North Dakota, USA, ICDD Granat-in-Aid.

[39] Dowty E. (1995). Shape for windows, version 5.0.1.

[40] Pujol M.C., Solé R., Massons J., Gavaldà Jna., Solans X., Zaldo C., Díaz F., Aguiló M. (2001). *J. Appl. Cryst*. 34:1

[41] Pokatilov E.P., Klimin S.N., Fomin V.M., Devreese J.T. (2002). *Phys. Review B*. *65*:075316-1

[42] Kaminskii A.A. (2003). *Phys. stat. sol. (a)* 2:215

[43] Griebner U., Petrov V., Petermann K., Peters V. (2004). *Opt. Express* 12:3125

[44] Petermann K., Fornasiero L., Mix E., Peters V. (2002). *Opt. Mater*. 19:67

[45] Eilers H., Tissue B.M. (1990). *Chem. Phys. Lett*. 251:74

[46] Laversenne L., Guyot Y., Cohen-Abad M.Th., Boulon G.(2001). *Opt. Mater*. 6:475

[47] Peters V. (2001). Growth and Spectroscopy of Ytterbium-doped sesquioxides, Dissertation (Shaker Verlag, Aachen, Germany, www.shaker-online.com)

[48] Steckl A.J., Birhahn R. (1998). *Appl. Phys. Lett.* 73:1700

[49] Wu H., Poitras C.B., Lipson M., Spencer M.G., Hunting J., DiSalvo F.J. (2005). *Appl. Phys. Lett.* 86:191918

[50] Kikuchi A., Kawai M., Tada M., Kishino K. (2004). *Jpn. J. Appl. Phys.* 43:L1524

[51] Johnson J.C., Choi H.J., Knutsen K.P., Schaller R.D., Yang P., Saykally R.J. (2002). *Nature Mater.* 1:106

[52] Carvajal J.J., Aguiló M., Díaz F., Rojo J.C. (2007). *Chem. Mater.* 19:6543

[53] Diecke G.H., Crosswhite H.M. (1963). *Appl. Opt.* 2:675

[54] Krivolapchuk V.V., Lundin V.V., Mezdrogina M.M., Nasonov A.V., Rodin S.V., Shmidt N.M. (2004). *Phys. Solid State* 46:836

[55] Qin X., Yokomori T., Ju Y. (2007). *Appl. Phys. Lett.* 90:073104

[56] Ragan R., Kim S., Li X., Stanley Williams R. (2005). *Appl. Phys. A.* 80:1339

[57] Wang Z., Coffer J.L. (2002). *Nano Lett.* 2:1303

[58] Hirte T., Sasaki S., Li W., Miyashita H., Kimpara T., Satoh T. (2005). *Thin Solid Films* 487:35

[59] Satyanarayan M.N., Deepthy A., Bhat H.L. (1999). *Crit. Rev. Solid State Mater. Sci.* 24:103

[60] Peng L.-H., Hsu C.-C., Ng, J., Kung A.H. (2005). *Appl. Phys. Lett.* 84:3250

[61] Canalias C., Pasiskevicius V., Fokine M., Laurell F. (2005). *Appl. Phys. Lett.* 86:181 105

[62] Lehmann V., Föll H. (1990). *J. Electrochem. Soc.* 137:653

[63] Thomas P.A., Glazer A.M., Watts B.E. (1990). *Acta Crystallogr., Sect. B: Struct. Sci.* 46:333

[64] Galli M., Agio M., Andreani L.C., Belotti M., Guizzetti G., Marabelli F., Patrini M., Bettotti P., Dal Negro L., Gaburro Z., Pavesi L., Lui A., Bellutti P. (2002). *Phys. Rev. B: Condens. Matter Mater. Phys.* 65:113 111

[65] "Translight" software package by A. L. Reynolds, University of Glasgow, 2000.

[66] Sakoda K. (2001). *Optical Properties of Photonic Crystals*, Springer, Berlin, p. 111

[67] Peña A., Di Finizio S., Trifonov T., Carvajal J.J., Aguiló M., Pallarès J., Rodriguez A., Alcubilla R., Marsal L.F., Díaz F., Martorell J. (2006). *Adv. Materials* 18:2220

About the authors

Francesc Díaz *is Full Professor of Applied Physics at the* Universitat Rovira i Virgili (URV). *Since its foundation in 1996 to the present he has been Coordinator of the Physics and Crystallography of Materials (FiCMA) research group of URV. He has published 176 ISI papers, 4 books, 3 patents and more than 40 chapters of books. He is currently focussed in nanostructuring of optical materials, spectroscopy and lasing of rare-earth ions in crystalline hosts.*

Magdalena Aguiló *is Full Professor of Crystallography at the* Universitat Rovira i Virgili (URV)*. Since its establishment in 1996, she has been Coordinator of the Physics and Crystallography of Nanomaterials (FiCNA) research group of URV. She has published 140 ISI papers, 1 book, 2 patents and more than 10 chapters of books. Her research interests include crystal nucleation, X- ray diffraction, X-ray texture analysis and physical properties of materials in relation with their crystalline structure.*

Joan J. Carvajal *is Ramon y Cajal Researcher at the* Universitat Rovira i Virgili (URV). *He is member of the Physics and Crystallography of Nanomaterials (FiCNA) research group of URV. He is author of 30 ISI papers, and 5 book chapters. His research interests include synthesis and crystal growth of optical and semiconductor materials at the micro- and nanoscale for photonic applications using different technologies such as high-temperature solutions, chemical vapor deposition and growth by sol-gel methods.*